

Cleaning the Planck 2015 Sky Maps to Reveal the CMB Anisotropy

Ana Hoban* and Harper Sewalls†
(PHYS 321 Collaboration)
(Dated: April 14, 2020)

Making accurate maps of the Cosmic Microwave Background (CMB) is of great interest to the field of cosmology as it allows us to model and understand the early Universe. In this paper, we present three methods for cleaning away foreground interference from the microwave sky measurements of the Planck 2015 data. All of our methods involve finding linear combinations of the 9 frequency channels that the satellite measured to cancel out the foreground contamination from the galactic plane. We clean the data by breaking the sky up into separate regions (I), and by considering the different angular scales that contamination happens on, using spherical harmonic decomposition(II), as was done previously by [1],[2]. We also explore another approach (III), inspired by (II). We compare our cleaned maps to the Planck 2015 data analysis release and the maps' angular power spectrum with the known CMB power spectrum in order and find that the third method is most similar to the accepted power spectrum and CMB map.

I. INTRODUCTION

The discovery of the cosmic microwave background radiation (CMB) in 1965 has marked the beginning of a new era of cosmology. Not only did it hold the promise of offering an understanding of the primordial times of the Universe (around 380,000 years after the Big Bang), but also confirmed the inflationary model of the early Universe.

To investigate the CMB fluctuations, the Cosmic Background Explorer (COBE), the Wilkinson Microwave Anisotropy Probe (WMAP) and the Planck probe were sent to map the sky in all directions. Gaining more and more sensitivity to the temperature variations, each mission provided more precise and accurate mapping of the CMB.

To obtain such maps, the probes scanned the entire microwave sky at several frequencies. Although looking at the sky in this range is crucial to detect the anisotropies of the early Universe, it also reveals a lot of microwave emissions from the Milky Way and point sources across the sky. Including free-free, synchrotron, thermal dust as well as spinning and magnetic dust emissions, all the unwanted signals are grouped under the umbrella term “foreground emission” [2].

Mapping and analysing foreground [2] is useful to gain insight about radio sources of our galaxy as well as a better understanding of some physical processes. However, obtaining clean CMB maps is crucial into answering key cosmological questions about the primordial times as well as the evolution of our universe.

In this paper, we will investigate three methods of cleaning the foreground emission away and compare the resulting maps to discuss the differences between the

three approaches. We use the Planck 2015 data from [3], which was dipole-free prior to our analysis.

First, we adapt *Bennett's et al.* [2] method of region splitting, then we follow *Tegmark's et al.* [1] spherical harmonics method (SHMI). Finally, we explore a third method (SHMII), inspired by *Tegmark's et al.*, which can be viewed as an immense simplification of the second one SHMI.

II. METHODS OF MAP CLEANING

The data from [3] is split over 9 frequency channels: 30, 44, 70, 100, 143, 217, 353, 545, 857 GHz. The first seven were given in units of K_{cmb} whereas the last two were in MJy/sr. This is due to the instrumentation of the Plack satellite itself which has two detectors [4] that work differently, the Low Frequency Instrument (LFI) which can only look at the sky in the three first frequencies' range and the High Frequency Instrument (HFI) for the rest. The 100 to 353 GHz were already converted to K_{cmb} in [3], and we used [5] to obtain the right units for the two highest bands.

A. Region Splitting Method

There are two parts to this method of isolating the CMB from the foreground contamination. The first is splitting the sky into regions by quantifying the amount of foreground interference in each. The second is finding the weights for each frequency channel such that the linear combination of weighted channels is the cleaned map for a given region.

The region splitting is the same as what *Tegmark et al.* does to decide what parts of the map have similar kinds of interference. We chose this over the *Bennett et al.* method since it doesn't make assumptions about which frequency channel is most foreground contaminated. The nine frequency channels each have the temperature of all

* ana.hoban@mail.mcgill.ca; Physics Department, McGill University.

† harper.sewalls@mail.mcgill.ca; Physics Department, McGill University.

the 3,145,128 sky pixels based on intensity of the light (this is done by assuming a black body emission spectrum). The adjacent temperature regions are subtracted from each other (30-44 GHz, 44-70GHz, ..., 857-545GHz) and the maximum absolute value for each point in the sky is taken as the junk map value for that pixel. The regions are then decided by taking contours of the junk map that are logarithmically evenly spaced, from the smallest junk map pixel value to the largest. This junk map method allows the CMB signal to be effectively removed and the magnitude of the foreground to shine through.

Once the region splitting has been decided, we take each frequency channel and cut out all of the temperature values that aren't in that region. Now we have a list $T(\nu_i, \hat{r})$, where ν_i is the frequency channel and \hat{r} is a pixel within the region. Since the CMB has very low variance over the sky compared to the foreground emission, we would like to find channel weights \mathbf{w} such that the variance of the combined map

$$T_{clean}(\hat{r}) = \sum_{i=1}^9 \mathbf{w}_i T(\nu_i, \hat{r}) \quad (1)$$

is minimized. The trivial solution is setting $\mathbf{w} = \vec{0}$, but then $T(\nu_i, \hat{r}) = 0$ and thus we would destroy the CMB. We then impose the restriction that

$$\sum_{i=1}^9 \mathbf{w}_i = 1 \quad (2)$$

and by doing this, we also preserve the CMB temperature (since the CMB temperature is independent of frequency but the foreground isn't). Minimizing the variance of Eq. 1 subject to the restriction of Eq. 2 gives us a formula for the weights. This formula, derived from the method of Lagrange multipliers [6], is given by

$$\mathbf{w}_i = \frac{\mathbf{H}^{-1}\mathbf{e}}{\mathbf{e}^T \mathbf{H}^{-1}\mathbf{e}} \quad (3)$$

where \mathbf{e} is the unit vector of length 9, and \mathbf{H} is a 9×9 matrix defined by

$$\mathbf{H}_{ij} = \sum_k T(\nu_i, \hat{r}_k) T(\nu_j, \hat{r}_k). \quad (4)$$

Eq. 4 is a sum over the whole region. Once these weights are computed in this way for each region, they are applied using Eq. 1 and then the regions are recombined into a single map as in Fig. 1.

B. Spherical Harmonic Method 1 (SHMI)

For SHMI, we used an adaptation of the spherical harmonic splitting described by *Tegmark et al.* The main difference between what is described by *Tegmark et al.* and us is that we do not split the CMB into regions for

the spherical harmonic cleaning. The advantage of this method is that we are able to clean the map at different angular resolution scales. Foreground interference from dust tends to have lower angular resolution than instrument noise, but both need to be cleaned from the data. Spherical harmonic functions are like sines and cosines, but defined on the sphere. Thus, they can be used as a basis for well-behaved functions, and by decomposing a spherical function into its spherical harmonic parts, we are essentially doing what a Fourier series does to a periodic one dimensional function [6]. The equations to transform from real space to spherical harmonic space is

$$a_{\ell m}^i \equiv \int Y_{\ell m}(\hat{r})^* T(\nu_i, \hat{r}) d\Omega \quad (5)$$

where $Y_{\ell m}$ are the spherical harmonic functions and the integral is over the whole sky. The equation to transform from spherical harmonic space to real space is

$$T(\nu_i, \hat{r}) = \sum a_{\ell m}^i Y_{\ell m}(\hat{r}) \quad (6)$$

where the sum is over all of the ℓ and m that are being used for the spherical harmonics.

We use spherical harmonic orders $\ell = 0$ to $\ell = 1024$. The first step is to compute a 9×9 cross-power spectrum matrix for each ℓ . Each matrix is defined by

$$\mathbf{C}_\ell^{ij} = \langle \mathbf{a}_{\ell m}^i * \mathbf{a}_{\ell m}^j \rangle \quad (7)$$

where the $\mathbf{a}_{\ell m}^i$ are the spherical harmonic coefficients from the i th channel. Now we have 1025 matrices (one for each ℓ) that we denote \mathbf{C} . Now we compute weights for each ℓ using an equation with the same form as equation 3 as follows

$$\mathbf{w}_\ell = \frac{\mathbf{C}_\ell^{-1} \mathbf{e}}{\mathbf{e}^T \mathbf{C}_\ell^{-1} \mathbf{e}} \quad (8)$$

where \mathbf{e} is the unit vector of length 9 and \mathbf{w}_ℓ is the 9 dimensional weight vector for the ℓ th spherical harmonic.

To weight the channels and recombine, we transform each frequency map into spherical harmonic space and then apply weights as follows

$$a_{\ell m} = \sum_{i=1}^9 w_\ell^i \frac{a_{\ell m}^i}{B_\ell} \quad (9)$$

where w_ℓ^i is the weight of the i th channel at harmonic order ℓ and B_ℓ is the beam function [7] computed by Healpy [8] which corrects for the pixelation of the maps affecting the calculation of spherical harmonic coefficients. From here we use Eq. 6 to bring the map back into real space and plot it on the whole sphere.

C. Spherical Harmonic Method II (SHM2)

This method was greatly inspired by *Tegmark et al.*'s spherical harmonics approach. However, there exist huge

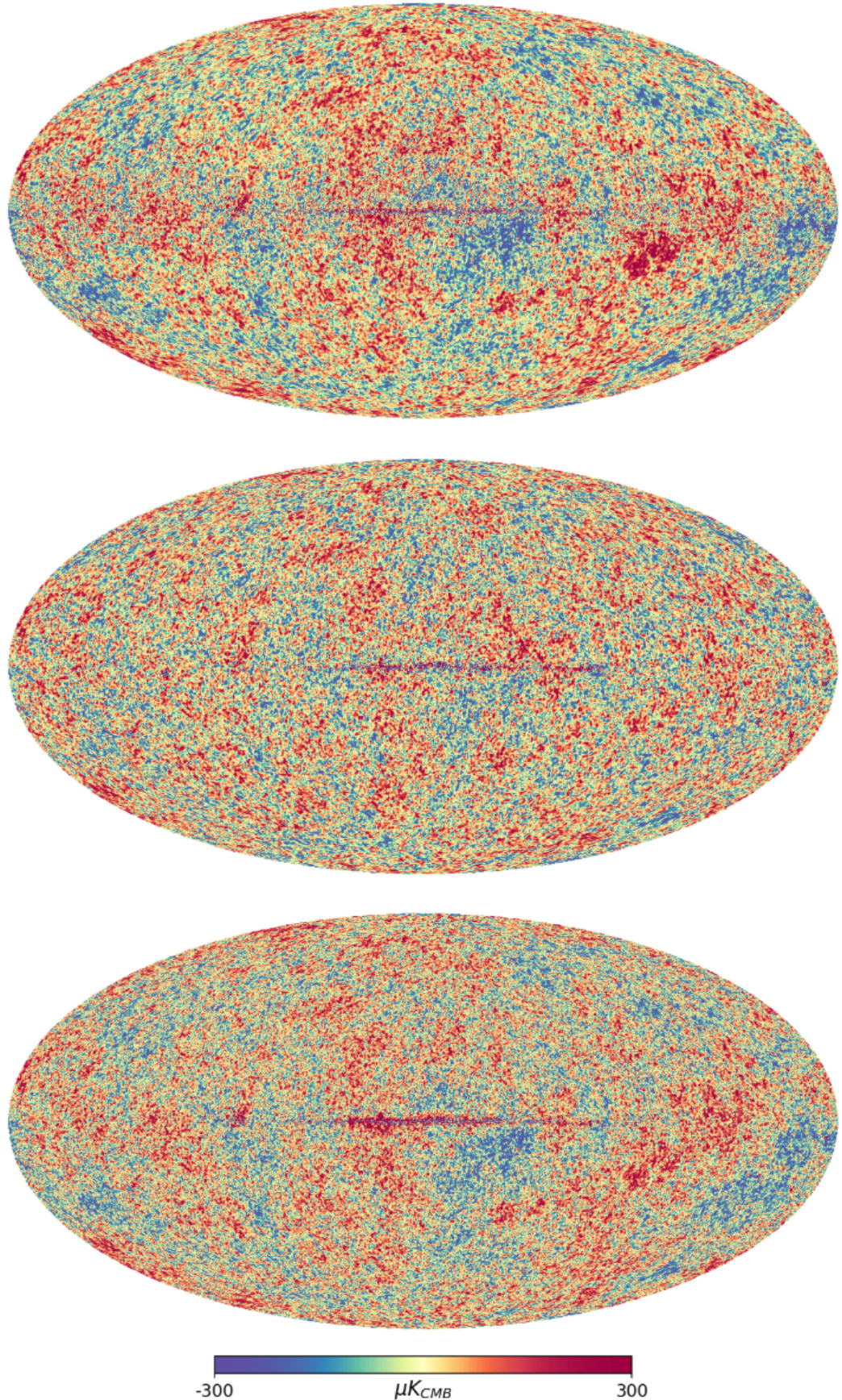


FIG. 1. The three final cleaned maps from the RSM (**top**), SHMI (**middle**) and SHMII (**bottom**). To see the maps in better resolution, see the git repo.

differences between both methods which appear to almost contradict the essence of SHMI; to mostly work in spherical harmonics, to find the cross-power spectrum and weights for each ℓ and form the final map from the weighted $a_{\ell m}$'s. In fact, this method unexpectedly works well despite its simplicity.

First, a cross-power spectrum matrix is computed using Eq. 8. The resulting $9 \times 9 \times 1025$ list of matrices, was reduced to a two-dimensional matrix $\mathbf{C}_{9 \times 9}$ by averaging over the ℓ 's for each combination of i and j according to the following:

$$\mathbf{C}^{ij} = \frac{1}{\ell_{max} + 1} \sum_{\ell=0}^{\ell_{max}} \frac{1}{2\ell + 1} \sum_{m=-\ell}^{\ell} (\mathbf{a}_{\ell m}^i * \mathbf{a}_{\ell m}^j). \quad (10)$$

The inner average (all the $C_{ij\ell}$'s) was computed using the Anafast function from the Healpy [8] package. The outer sum was computed manually.

The final map was formed by a linear combination of the 9 frequency maps using the weights that were computed with Eq. 8 with $\mathbf{C}_\ell = \mathbf{C}_{9 \times 9}$, as follows:

$$\sum_{i=1}^9 w_i T(\nu_i, \hat{r}) \quad (11)$$

where w_i is the weight of frequency channel ν_i .

III. RESULTS AND DISCUSSION

All the results that follow were optimized to resemble Fig. 3 and the CMB's known power spectrum [9], plotted in Fig. 6 as much as possible. Producing the best plots for each method was achieved by tweaking small details through trial and error. As a general rule, we found that imposing galactic cuts makes the plots and resulting power spectra worse, and downgrading the junk map resolution for RSM makes the plots worse. Additionally, every result was optimized when the data was handled in μK_{cmb} (i.e. factor of 10^6 applied on the raw data).

A. Region Splitting Method

For the RSM we experimented with changing the number of regions being used to see which one would give the best map. Four representative maps are shown in Fig. 2. We found little difference in the maps produced from this type of region splitting visually, as well as power-spectrum wise. The eleven-region map was chosen to represent the RSM in the rest of the paper, as the improvement is negligible in maps with larger numbers of regions. The power spectra for these four maps are identical, thus were not included (they look like the RSM curve in Fig. 6). The thickness of the galactic center is slightly smaller in the 7, 11, and 15 region maps than in

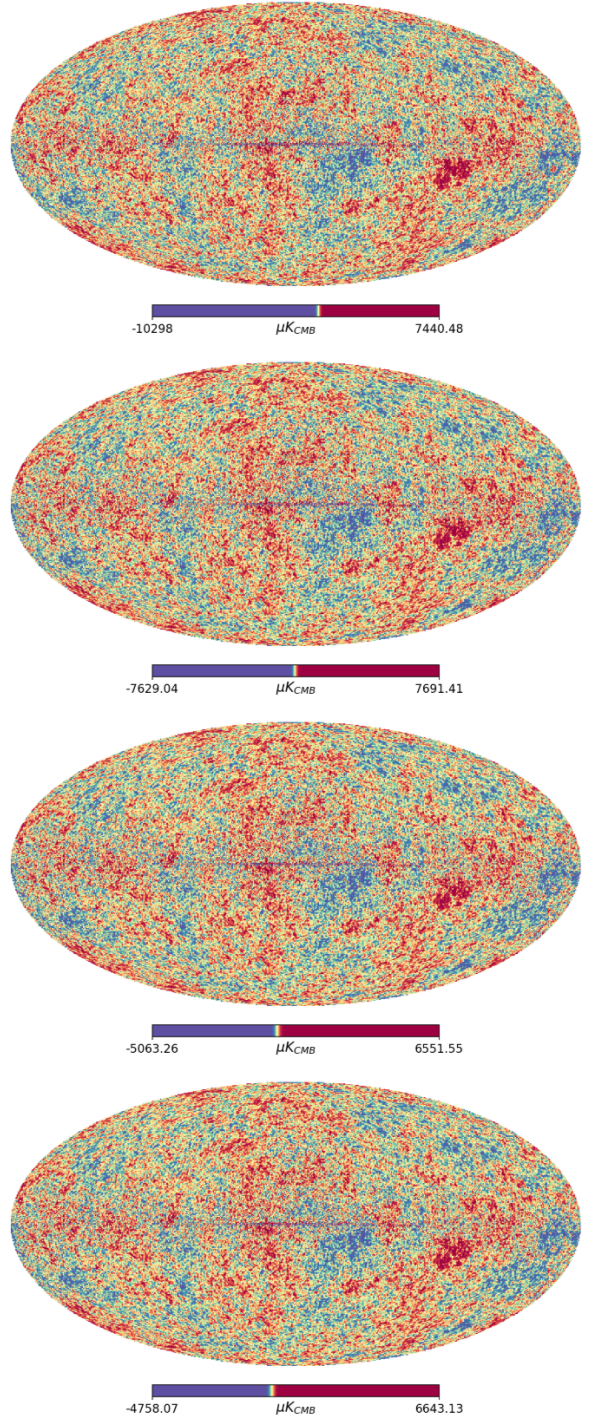


FIG. 2. Cleaned maps for different numbers of regions (from RSM), respectively 3, 7, 11 and 15 from top to bottom.

the 3 region map. This is probably due to the fact that in the latter, the galactic center is contained in a region that is pretty large, so it is not isolated in its own region. The weights for the region that contain the galactic center have to account for more than just the huge temperature spike at the galactic center, and thus they more poorly cancel out the galactic center.

B. Comparing Methods

Maps

The final cleaned maps for the three methods are shown in Fig. 1. Visually, when compared to the originally cleaned maps from the Planck data in Fig. 3, all maps appear to be cleared from any foreground coming from the galactic plane, except for that small line in the middle which we were unable to remove.

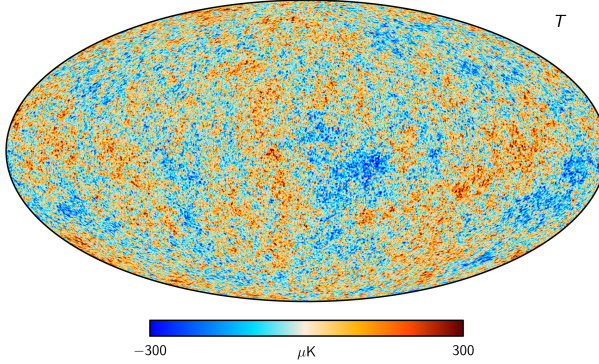


FIG. 3. Original cleaned Planck map obtained from [10].

The top map (RSM) in Fig. 1 seems to have less small-scale structure than the two below (SHMI&II) as well as more area with the extreme blue and red colors. In other words, the coldest and hottest spots are more visible in the top map than in the bottom two. It makes sense that the methods in which spherical harmonic coefficients were used yield maps in which details at smaller angular resolutions are visible, since using large ℓ values ensures the small fluctuations are accounted for.

Another striking difference between the maps is the uniformity of the map obtained by SHMI (middle of Fig. 1). Although it resembles the original Planck map, it also displays what almost seem like random statistical fluctuations in regions we would expect only blue or red pixels. For instance, this problem is evident in the southern hemisphere in what is supposed to be a large blue area, right below the center of the galactic plane, and in the even larger red extended area.

This is very surprising as spherical harmonics were expected to work well due to their sensitivity to small angular scales. One reason this method may not have worked as well as in *Tegmark et al.*, is that we did not use region splitting in tandem with spherical harmonics unlike the *Tegmark et al.* group. Thus, region splitting could be a way of fixing this discrepancy between this map and the original Planck one, or at least lower it.

Weights

Another way to look at the differences between the three maps we obtained is by comparing the weight as-

signed to each frequency channel.

Fig. 4, shows the set of weights for each ℓ in SHMI, it is clear that for all ℓ 's, highly contaminated maps like the 353, 545, 857 GHz ones count the least in making the final map. That is expected, because CMB anisotropies are less contaminated by foreground emission in the lower frequency range ($\sim 30\text{-}150$ G Hz) [2].

It is also clear that for small ℓ 's, the weighting is very extreme: both very high and very low values are generated. This may be due to large variations in the foreground multi-pole moments for different frequency channels. In other words, the quadripole may be very strong for the first two channels, but it may not contribute much to the other channels, so the relative weight of the quadripole moment for the first few channels might need to be larger than the other channels in order to cancel each other out. Then, for medium-sized fluctuations, channels 3 and 5 seem to cancel each other out whereas channels 1, 2, and 4 are all slightly positively contributing to the final map. As channels 3, 4, and 5 are visually the most foreground-deprived raw data maps, it is not surprising that they contribute most to the making of the final map.

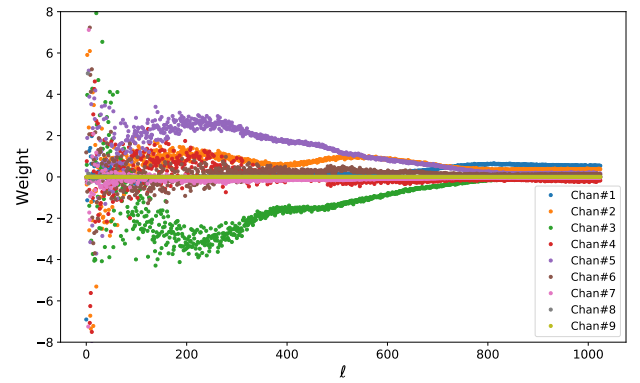


FIG. 4. Weighting of frequency channels for each ℓ as computed in SHMI. This is a zoomed in version of the plot, in the original, the weights for the first few ℓ 's cover a range of $\sim [-250,200]$.

In Fig. 5, we compare the weighting sets for RSM and SHMII. One feature to note is that, once again, we have tiny contributions from the two highest bands, which is expected since they are the most contaminated maps. Also, all the weights are in the same range for each channel, so these two methods (RSM&SHMII) are roughly consistent with each other. Otherwise, there are no meaningful similarities between the weight sets from the two methods.

Comparing Figs.4 and 5 highlights that for high (>500) ℓ the range of the weights in Fig. 4 is very similar to that of Fig. 5. This means that these methods yield similar weights in the higher ℓ region to the methods that don't care about particular values of ℓ . We expect this since

RSM and SHMII treat all ℓ values equally while there are more ℓ 's that correspond to medium-to-small-scale fluctuations (sub degree resolution) than lower resolution fluctuations of smaller ℓ values.

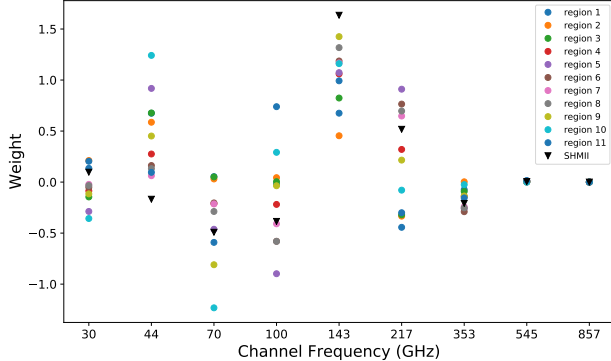


FIG. 5. Weighting of frequency channels for the RSM as well as the SHMII. The former method computed a set of weights for each region, each with a different color in the plot. The latter found only one set of weights for the whole map.

Power Spectrum

Even though this entire process was not as precise or accurate as other papers, we wanted to simply and more quantitatively determine which method worked best using the power spectrum of each cleaned CMB map.

Fig. 6 compares the power spectrum from each method's cleaned map to the currently accepted model. The power spectra were obtained by using the Anafast function from the Healpy [8] package with imposed galactic cuts to reduce galaxy interference in the spectrum. As expected, the biggest cut was made to the CMB map with the biggest foreground line along the galactic plane: the SHMII cleaned map.

Oddly, only SHMII produced a map for which the power spectrum resembles the model. Until $\ell \approx 900$ our curve follows that of the model very closely. On the other hand, RSM and SHMI's power spectra seem to agree with the model for the first oscillatory peak, but flatten at higher values of ℓ . This result is very unexpected since SHMI, in which each ℓ value was cleaned separately, was initially the most promising method. However, it does not visually look similar to Fig. 3 as we hoped, and it also does not match the power spectrum curve very well.

We are still unsure why SHMII works so well, but will suggest two possible explanations for its success.

First, SHMII is very different from SHMI since it only computes one set of weights, from an ℓ -independent matrix \mathbf{C} . We can interpret C^{ij} , with $i = j$, as reducing the anisotropy over all ℓ 's over the whole sky to a single number for channel i. When feeding \mathbf{C} into Eq. 3

we compute weights that minimize the overall average anisotropy of the weighted sum of the channels over the whole sky, while still ensuring Eq. 2 holds. Of course the CMB has its own anisotropy, but it is much smaller than the anisotropy of the foreground emission, which varies greatly over the sky (highly anisotropic). In other words, when considering the foreground's anisotropy, the CMB's becomes negligible. Therefore, in minimizing this average value, we are able to minimize the average foreground anisotropy and allow the CMB to dominate.

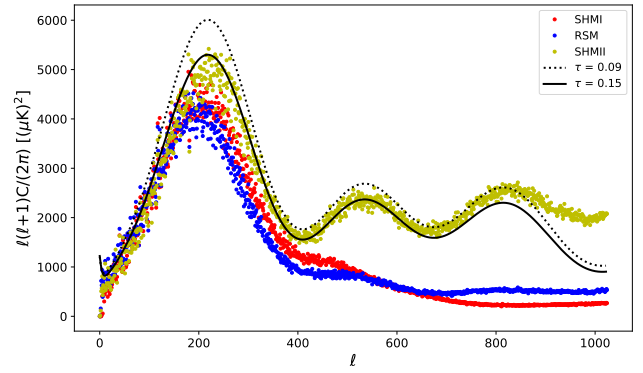


FIG. 6. Scaled CMB power spectrum from each final map from Fig. 1. The black curves are considered as the “model” and were obtained from prior observations and parameter fitting [11]. The full and dotted lines respectively represent the model with an optical depth, $\tau = 0.09$ and $\tau = 0.15$. Galactic cuts between latitudes of $\pm 3^\circ$, $\pm 3^\circ$ and $\pm 9^\circ$ were applied respectively to RSM, SHMI and SHMII.

The key to the second explanation lies in Eq. 10 as well. By averaging over the ℓ 's, we are favoring higher angular resolutions more than lower ones. Since $\ell \sim \frac{180^\circ}{\theta}$, we can intuitively see that there is less difference between two adjacent high ℓ values, e.g. 1000 and 1001, than between two adjacent low ℓ values, e.g. 4 and 5. Therefore, \mathbf{C} 's entries show how correlated the maps are between each other, over all the ℓ 's in most general way. Passing this “covariance” matrix through the weight finding Eq. 8 then minimizes the average variance of the sky pixels over all angular resolutions. In the eyes of the minimization process, all ℓ values are equally important, so the simple task of finding one single set of weights favors small-scale fluctuations (big ℓ), which are dominant when considering the average whole set of ℓ 's. Since the CMB happens small scale, it is greatly favored by this method, whereas the foreground, showcasing big scale features, is removed.

IV. CONCLUSION

The goal of this work was to produce clean CMB maps from the Planck 2015 data by removing foreground us-

ing different methods. We presented three distinct approaches: region splitting inspired by *Bennett et al.* [2], spherical harmonic cleaning following *Tegamark et al.* [1], and an adaptation of the latter method.

Overall, the most effective method was the third one, referred to as SHMII throughout the paper. This is the case both because the map is most similar to the professionally cleaned Planck map, and because it reveals a beautiful power spectrum that agrees with the current model.

These three different methods of CMB map cleaning were not intended to be as extensive as [1] and [2], and

so can be improved in many ways. For instance, one could more carefully follow *Tegmark's et al.* procedure and split up the maps into regions before applying the spherical harmonic method on each one. We could have also cut out the bright galactic center by statistically interpolating a patch that resembles the CMB to cover up this part of the map, which would in turn improve the resulting power spectrum. We could also use an MCMC to investigate how these cleaned maps would update parameters such as cosmological constants (e.g. the dark matter and energy ratios), and the Universe's primordial conditions (e.g. B_s , ω_s , Θ_s) [11].

-
- [1] T. et al., A high resolution foreground cleaned cmb map from wmap, Phys.Rev.D68:123523 , 15 (2003).
 - [2] B. et al., First year wilkinson microwave anisotropy probe (wmap) observations: Foreground emission, The Astrophysical Journal Supplement Series , 21 (2003).
 - [3] Planck public data release 2 maps, IRSA archive () .
 - [4] The Planck Mission kernel description, <http://planck.cf.ac.uk/mission> (), accessed: 2020-04-13.
 - [5] P. C. P. et al., Planck 2013 results. ix. hfi spectral response, Astronomy Astrophysics , 27 (2003).
 - [6] A. Liu, McGill phys 321 course notes (Winter 2020).
 - [7] P. C. et al., Planck 2015 results - iv. low frequency instrument beams and window functions, Astronomy Astrophysics (2016).
 - [8] Healpy documentation, online, version 1.12.10.
 - [9] LAMBDA kernel description, https://lambda.gsfc.nasa.gov/toolbox/tb_camb_form.cfm, accessed: 2020-04-13.
 - [10] E. S. Agency, Esa cosmos wiki 2018 cmb maps.
 - [11] L. Xu, Y. Wang, and H. Noh, Unified dark fluid with constant adiabatic sound speed and cosmic constraints, Physical Review D **85** (2011).